

Experimental Dynamic Stability Investigation on Orion Entry Capsule in Supersonic Flow

M. Sargolzaie¹, H. Fazeli^{2†} and M. R. Soltani³

¹ Aerospace Engineering, Aerospace Research Institute, Tehran, Iran

² Faculty of Mechanical Engineering, Malek Ashtar University of Technology, Tehran, Iran

³ Department of Aerospace Engineering, Sharif University of Technology, Tehran, Iran

†Corresponding Author Email: fazeli@mut.ac.ir

ABSTRACT

Re-entry capsules' success depends significantly on dynamic and static stability, particularly before deploying the main parachute. Determining the range of dynamic instability and investigating the underlying causes is crucial for designing the entry capsule's control system. Dynamic stability is analyzed in this study based on pitch moment coefficients obtained from forced oscillation experiments conducted in the trisonic wind tunnel for the Orion entry capsule. The results reveal that pressure fluctuations at the aftbody of this model begin at Mach 2. The findings and other research results emphasize the significant role of the aftbody geometry in generating dynamic instability at low supersonic speeds due to its interaction with vortex flow. The results also demonstrate that increasing the Mach number to 2.2 would result in a near zero-pressure coefficient on the capsule's aftbody, which implies that there is no acting force on the aftbody. The results show that as the freestream Mach number increases from $M_\infty = 1.8$ to $M_\infty = 2.2$, the pressure on the aftbody remains unchanged during the pitching motion due to approaching the shear layer towards the body and consequent shrinking of the aftbody vortex. Furthermore, the sensitivity of dynamic stability to the mean angle of attack was investigated. It is shown that a slight increase of approximately 5 degrees in the mean angle of attack can considerably enhance the re-entry capsule's dynamic stability.

Article History

Received May 14, 2024

Revised November 10, 2024

Accepted December 14, 2024

Available online March 4, 2025

Keywords:

Dynamic stability

Entry capsule

Supersonic flow

Experimental aerodynamic

Force oscillation

1. INTRODUCTION

In the pursuit of sending humans to space, ensuring a safe return has remained a paramount concern. Returning capsules are beset by challenges encompassing heat management, communication, and control throughout their voyage until they reach the Earth's surface. Re-entry capsules often employ blunted geometries to contend with issues of intense heat. Drawing from accumulated experiences to date, most of these geometries exhibit inherent dynamic instability within specific speed ranges. Addressing this issue requires rectifying the investigated geometries' dynamic and static behavior. Static stability refers to how quickly the capsule returns to its original state, and dynamic stability considers the changes over time as it returns to its equilibrium state. In other words, static stability measures the immediate response, while dynamic stability looks into the capsule's entire behavior after a disturbance. For more explanation of the dynamic stability of the entry capsules, [Kazemba et al. \(2012\)](#) presented a comprehensive description of this research

area.

Due to the absence of the main aerodynamic control surfaces, such as wings and tails on re-entry capsules, it is crucial to determine and manage the aerodynamic forces and moments throughout the return phase. Designers of the entry capsule might also employ auxiliary mechanisms such as flaps, reaction control systems (RCS), or drogue chutes for fast response to disturbances. Furthermore, achieving a targeted landing site for expedited rescue operations mandates precise control over the capsule's trajectory.

The complex interaction of massive vortex flow with other parameters in an unsteady supersonic flow within a blunt capsule, coupled with our limited understanding of the governing physics, necessitates numerical and experimental investigations to determine the dynamic stability of re-entry capsules.

Parameters influencing dynamic stability can be divided into two general categories: geometrical attributes

NOMENCLATURE			
M_z	Pitching Moment	α_p	Pitch Angle
F_N	Normal Force	ω	Angular Speed
D_{ref}	Reference Length (maximum Diameter)	f	Frequency of Pitch Oscillation
U_∞	Freestream Velocity	α_{max}	Amplitude of Pitch Oscillation
M_∞	Freestream Mach Number	$Cm_q + Cm_{\dot{\alpha}}$	Pitch Dynamic Stability Coefficient
C_p	Pressure Coefficient	t	Time

of the capsule and environmental factors such as Mach number, oscillation frequency, oscillation amplitude, and mean angle of attack. Overlooking the impact of any of these parameters during the design phase can lead to inappropriate landing. Notably, Ballistic range tests stand as the world's most reliable method for ascertaining the dynamic stability of vehicles.

Our literature survey shows that one of the pioneering studies in the field of stability analysis and simulation has been performed by [Bird and Reese Jr \(1958\)](#). They used an analytical method and discussed geometric attributes related to the stability of entry bodies. [Fletcher \(1960\)](#) has investigated experimentally the influence of Mach number ranging from 1.93 to 3.05 on the dynamic stability during pitch oscillation in a crewed capsule. [Dayman et al. \(1963\)](#) analyzed the effect of geometric shape parameters on damping large amplitude oscillations when entering Mars' atmosphere. [Steketee \(1967\)](#) investigated the dynamic stability of space vehicles and calculated important parameters for stability analysis and system control.

Due to the considerable costs and limitations associated with the experimental method, as well as the low accuracy of the analytical approaches, the research concentration focused on two main areas. First, the development centered on numerical simulation programs that offered appropriate accuracy, such as overflow software ([Benek et al., 1985](#); [Kandula & Buning, 1994](#); [Jespersen et al., 1997](#); [Liou & Buning, 2000](#)). Second, attention turned to exploring the effect of experimental wind tunnel equipment on dynamic stability outcomes ([Whitlock & Siemers, 1972](#); [Reding & Ericsson, 1972](#); [Uselton & Cyran, 1980](#)). [Teramoto et al. \(2001\)](#) simulated the dynamic stability of the Muses-C capsule at Mach 1.3 in forced oscillation conditions. This research highlighted the phase discrepancy between aftbody surface behavior and oscillation. [Cliff and Thomas \(2005\)](#) employed numerical and experimental methodologies to optimize the aerodynamic coefficients of the Apollo capsule, enhancing stability within a transonic flow.

[Schoenenberger and Queen \(2008\)](#) proposed an analytical solution to measure the dynamic stability of blunt bodies by defining a "limit cycle." They demonstrated that the lift curve's slope and the testing techniques' boundary conditions affect the damping coefficients. [Schrijer and Walpot \(2010\)](#) investigated the wake behind an Apollo-shaped capsule using schlieren and stereo particle image velocimetry. They provided a comprehensive overview of the 3D flow structure behind the capsule, including the shear layer, re-compression shock, and reflected bow shock. Interestingly, they found that as the Mach number decreases, the attached shear layer occurs at a higher angle of attack. [Owens and](#)

[Aubuchon \(2011\)](#) gathered test data from the Orion model, and they revealed that dynamic instability for this geometry occurs at approximately Mach 2.

[Kazemba et al. \(2012\)](#) presented a comprehensive review of this field by collecting and categorizing previous research results on the dynamic stability of entry capsules. In their study, Kazemba investigated the influencing parameters and explained the dynamic instability of blunt entry bodies. [Adamov et al. \(2016\)](#) examined the dynamic behavior of new entry geometries within the Mach 2 range using a free oscillation test, indicating the emergence of dynamic instability around Mach 1.8. That same year, a group of researchers at JAXA leveraged wind tunnel data and flight tests of the OREX capsule to study the dynamic behavior during the re-entry phase ([Matsumoto et al., 2016](#)). Subsequently, this group designed a controller for the capsule to navigate through dynamic instability before parachute deployment. [Yang and Radespiel \(2017\)](#) investigated the dynamic behavior of the Apollo entry capsule, analyzing the impact of front and back geometry on pitching moment behavior through numerical simulation.

[Brock et al. \(2019\)](#) explored dynamic stability through a Ballistic range test for an inflatable return capsule. Using numerical simulations, they investigated the pressure distribution behavior at several points. Notably, their study emphasized the substantial influence of the vortex trailing the capsule on dynamic stability. [Tsurumoto et al. \(2019\)](#) investigated the mechanism of aerodynamic instability for the Hayabusa-type capsule in transonic flow using in-house codes. They found that the capsule shoulder geometry can prevent aerodynamic instability by affecting the expansion area behavior. [Chasovnikov \(2020\)](#) studied the dynamic stability behavior of a re-entry capsule through free oscillation tests at Mach 2. He concluded that existing mathematical models were unsuitable for predicting behavior within this Mach range due to the nonlinearity. [Nagai et al. \(2021\)](#) investigated the dynamic stability of the JAXA entry capsule in transonic flow ($M_\infty=1.4$) by synergistic experimental and numerical works. They used experiments to provide information about the amplitudes and frequencies for numerical simulations involving forced oscillations to determine the stability behavior of a re-entry lifting capsule with a large aft section.

[Wei et al. \(2021\)](#) investigated the dynamic stability of the Tianwen-1 Mars entry capsule through a ballistic range test at the supersonic range. Their results indicated that the model in trimmed configuration is dynamically unstable at $M_\infty=1.5$. [Li et al. \(2022\)](#) proposed the integrated numerical simulation method and studied the dynamic characteristics of the Mars entry module across transonic

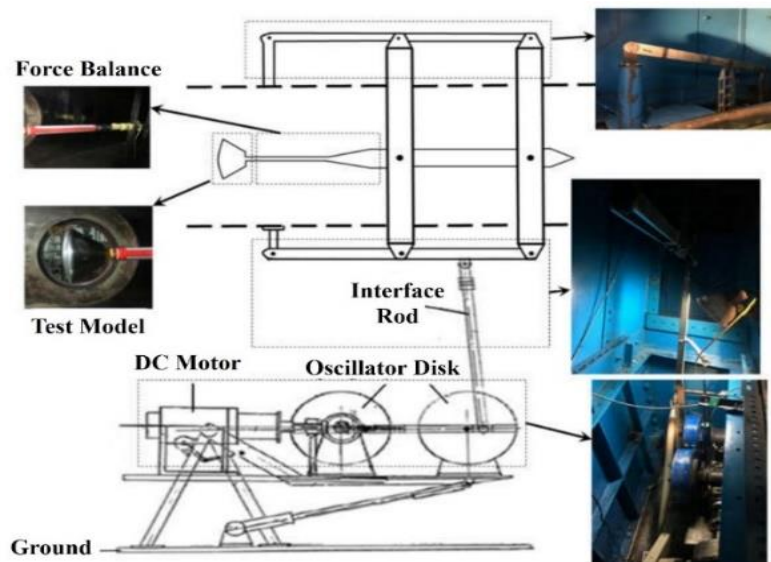


Fig. 1 Oscillation mechanism in the wind tunnel

to supersonic speeds. They specifically investigated the effect of different afterbody shapes on dynamic stability. [Mark and Netto \(2023\)](#) designed a cost-effective neural network for determining the dynamic stability of an entry capsule using the data collected during free fall tests. [Placco et al. \(2023\)](#) used high-fidelity time-evolving simulations (using LES and IBM techniques) for an entry capsule in a supersonic flight at different angles of attack. Their results enhanced our understanding of unsteady dynamics in this critical range. [Han et al. \(2024\)](#) investigated flow characteristics over a re-entry capsule using detached eddy simulation in transonic flow. They discovered that fluctuations in the free shear layer impact base pressure and affect the capsule's dynamic instability. [Kawano et al. \(2024\)](#) explored the oscillation behavior of an inflatable entry capsule in a transonic wind tunnel. They found that the capsule's back shape influences oscillation amplitude but not the overall trend of dynamic stability.

In conclusion of pre-mentioned literature, the experimental test results have been expressed in recent years using force coefficients and flow visualization, while numerical simulations present data in pressure coefficients and flow streamlines. Recent research indicates that dynamic instability in re-entry capsules occurs within the velocity range between high transonic and low supersonic speeds. To address the limitations of the experimental method in determining the dynamic stability mechanisms, we employed simultaneous data acquisition of force, pressure, and flow visualization. Notably, this data acquisition method is used for the first time in the re-entry capsule tests. This paper explores the dynamic stability of the Orion re-entry capsule operating in low supersonic flow conditions using simultaneous measurements of force balance and pressure sensors located on the model body. Also, the dynamic instability mechanism of this re-entry capsule has been elucidated by utilizing flow visualizations, along with the model's pressure measurements and the calculated pitching moment around the center of gravity (C.G.).

2. EXPERIMENTAL DETAILS

This section details the test infrastructure equipment, the data acquisition system, and the model geometry.

2.1 Test Infrastructure Equipment

The trisonic wind tunnel utilized for testing infrastructure features a square test section measuring $60 \times 60 \text{ cm}^2$ with a length of 1.4 m. Design specifications of this wind tunnel indicate a nominal Mach number range of 0.4 to 2.5, a Reynolds number between 37.6 and 70 million per unit meter, and a flow turbulence intensity between 0.4 and 1.4%. The tunnel walls incorporate apertures designed to extract the boundary layer. This suction process is facilitated by an ejector mechanism, effectively reducing the boundary layer thickness. As a result, the shock waves inside the wind tunnel become more stable, and the bow shock reflection from the tunnel walls is directed downward toward the diffuser. The model and its associated sting are adjusted for the static angle of attack and dynamic oscillation using a parallelogram oscillator mechanism (Fig. 1). The electrical motor responsible for the angle of attack manipulation is calibrated using a digital angle meter with an accuracy of ± 0.05 degrees. The pitch oscillation center of the model is determined by the frame's connection point to the test section walls. A Z-type Schlieren system is used to visualize flow phenomena.

2.2 Test Model and Data Acquisition System

The wind tunnel test model, illustrated in Fig. 2, is based on a simplified geometry of the Orion re-entry capsule and features a blockage ratio of 2.96%. The model has been thoughtfully designed for ease of construction and internal access, resulting in a two-part structure crafted from 7000 series aluminum alloy. A series of 0.8 mm diameter holes facilitates pressure measurement across the body's surface. These holes are interconnected by tubes with pressure sensors situated within the model.

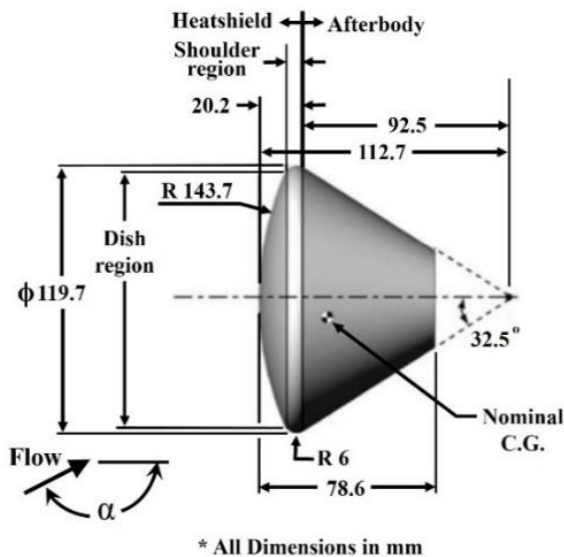


Fig. 2 The geometry of the test model

The pressure sensors, exhibiting a measurement accuracy of 0.1 kilopascal (0.1% F.S.), are accompanied by a 16-channel data acquisition system capable of recording 5000 samples per second per channel. A dedicated battery unit is integrated into the model to ensure uninterrupted data recording, as shown in Fig. 3 (a). Also, the detailed arrangement of the sensor number and tap position is shown in Fig. 3 (b).

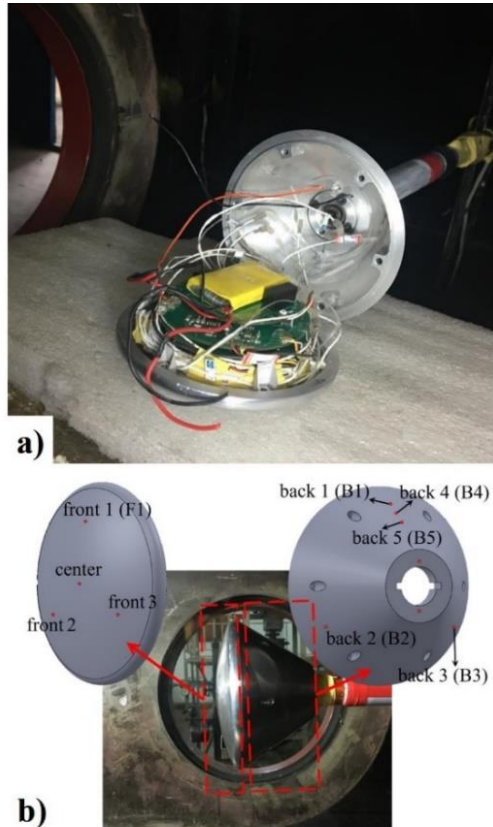


Fig. 3 a) The onboard data acquisition system, b) Schematic of pressure sensors on the surface of the test model

The pitching moment is measured using a five-component force balance. This balance, featuring dimensions of 363 mm in length and 22 mm in diameter, provides a calibration-based uncertainty of 0.266% for normal force and 0.513% for pitching moment measurements. The force balance and pressure sensors record data on the two separated data acquisition boards. Before each test, the testing apparatus undergoes calibration, including the balance, oscillator mechanism, and flow speed sensor. Correction coefficients from calibration are input into the wind tunnel controller and data acquisition software. During the test, balance output voltages are recorded, and force and moment magnitudes are calculated using pre-established calibration relationships. Throughout the tests, the prevailing total pressure and temperature maintained respective values of 840 mbar and 293 K. For the three experimental Mach numbers (1.8, 2, and 2.2), the Reynolds number of the model is approximately 6 million, 9 million, and 12 million, respectively.

Several factors contribute to potential errors in the obtained results. Among these factors are structural vibrations induced by the model's holder length and the connections between the holder and balance in the supersonic flow. Precise measurements are performed to minimize the impact of unlikely human-operator misjudgments and the boundary layer suction on the tunnel walls. These measures include reinforcing the structural integrity of the connections and framework, augmenting the maximum ejector suction within the test section, and employing synchronization triggers to harmonize balance and pressure data recording. In addition, guidelines were developed to enhance the accuracy of human operators involved in the procedures. To further reduce the impact of reflected shock waves originating from the tunnel walls on the balance situated behind the model, a tubular plastic shield, as depicted in Fig. 1, was employed. This shield fully envelops the balance, mitigating potential disturbances. The uncertainty of the measured parameters is reported in Table 1.

Data collection during each test case spanned 10 seconds. After calculating the normal force and pitching moment, as measured by force balance and oscillation angle, the raw data were de-noised through a time-averaging filter integrated into the MATLAB code.

Importantly, this filter preserves the inherent time trend of the data, ensuring consistency. The calculation of the dynamic stability coefficient for forced oscillation, as per equation (1), requires data encompassing a complete pitching moment cycle of oscillation centered on the mean angle of attack.

Table 1 Uncertainty of measured parameters (%)

$\Delta M_\infty / M_\infty$	$\Delta C m_q / C m_q$	$\Delta C_p / C_p$	$\Delta M_z / M_z$
1.46	3.7	1	0.513

Table 2 Input parameters of test and range of changes

Test input parameter	Range of change
Mach number	1.8, 2.0, 2.2
Static angle of attack	-2 ~ +7 °
Mean angle of attack in pitch oscillation motion	0, +5 °
Amplitude of pitch oscillation	2 °
Frequency of pitching motion	3, 4, 5 Hz

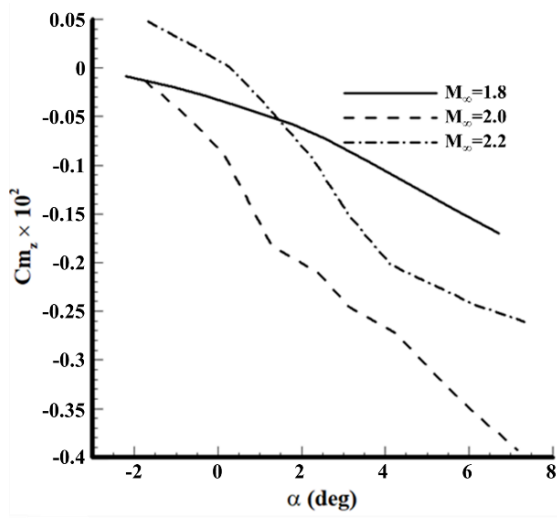


Fig. 4 Variations of pitching moment coefficient around C.G. in static tests

$$Cm_q + Cm_{m\dot{\alpha}} = \frac{2U_\infty \int Cm_z d\alpha}{D_{ref} \int \dot{\alpha} d\alpha} \quad (1)$$

A comprehensive averaging process was performed using data from all time cycles in each test case to facilitate this. The data obtained from the averaged cycle subsequently replaces the original data for that particular case. The extent of variations in test parameters across the

test cases is detailed in Table 2. The experimental tests began with a static motion configuration, followed by the implementation of forced pitching oscillations under the specifications outlined in Table 2.

3. RESULTS AND DISCUSSION

The pitching moment and pressure coefficient results were calculated using calibration methods after conducting tests in both static and oscillating states. The variations in pitching moment around the C.G. for three Mach numbers during static tests are depicted in Fig.4. An interesting observation emerges from the static flow field behavior at Mach 1.8, as shown in Fig. 5. A reflected wave originating from the tunnel walls in the initial segment of the balance interface might potentially affect the results, particularly regarding the angle of attack. Notably, the pitching moment coefficient at Mach 2.41, as depicted in Fig. 6 of [Yang and Radespiel \(2017\)](#), falls within the range defined by the results for Mach 1.65 and Mach 1.1. This intriguing finding raises the possibility of an unexplained physical phenomenon within this range. Currently, the available sources do not explain this phenomenon. Based on the author's knowledge, it can be assumed that this phenomenon may be related to the dynamic instability that occurs at Mach numbers less than 2. A more comprehensive investigation employing different geometries could illuminate this intriguing matter.

It is observed that two vertical reflecting waves originated from the tunnel walls (Fig. 5). As shown in [Gülhan et al. \(2011\)](#) and [Willems et al. \(2013\)](#), the two normal waves derive from the interaction of the bow shock in front of the model with the boundary layer on the tunnel walls. The bow shock and the boundary layer interaction generate a separation bubble. This bubble induces a sudden augmentation in the boundary layer's thickness along the walls. One potential approach to mitigating this effect involves augmenting the suction within the diffuser area and ejector, thus reducing the

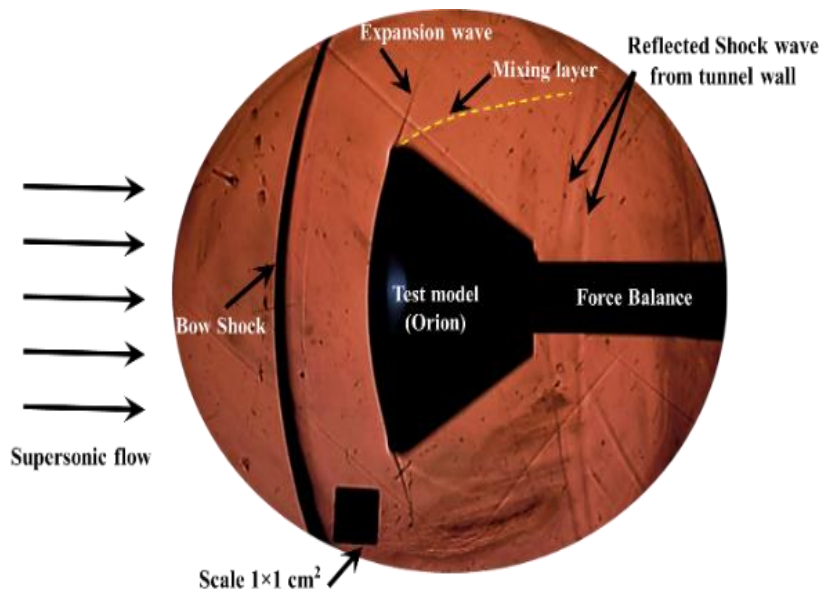
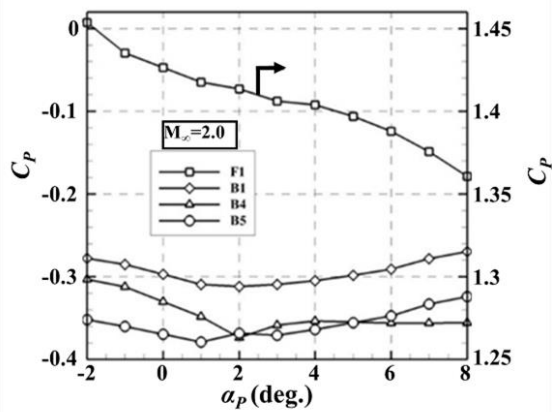
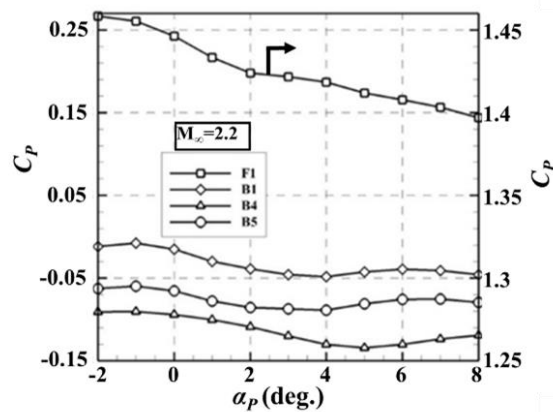


Fig. 5 Flow visualization of $M_\infty=1.8$ & zero angle of attack in the static test



a) pressure coefficient at $M_\infty=2.0$



b) pressure coefficient at $M_\infty=2.2$

Fig. 6 Changes of pressure coefficient vs. static angle of attack at Mach number

boundary layer thickness and propelling the two normal reflecting waves downstream. It is momentous to acknowledge that this phenomenon is an inherent limitation to the experimental testing of such geometries in walled supersonic wind tunnels. Given the potentially significant impact on changes in the pressure coefficient of the model's aftbody, our subsequent discussion will focus solely on the pressure coefficient behavior at Mach 2 and 2.2. These behaviors are illustrated in Fig. 6, which shows the pressure coefficient value for sensor F1 on the right axis alongside the values for the three sensors on the model's rear (B1, B4, and B5) on the left axis. As shown in Fig 6, two vertical axes represent changes in the pressure coefficient but at different values. The right axis values are for the front pressure sensor, indicated by an arrow line in Fig 6. At the same time, the left axis values are for the back sensors. The right axis values are the same in parts (a) and (b) of the figure—Meanwhile, the left axis value changes with the Mach number.

In Fig. 6, the front sensor (F1) recorded a decline in pressure with an increased angle of attack. This occurs because the stagnation region shifts downward in front of the model. As the angle of attack is reduced, the flow along the surface has more time to accelerate, leading to a decrease in static pressure. Conversely, the sensors positioned at the model's rear (B1 to B5) exhibit minimal alterations owing to the pronounced influence of

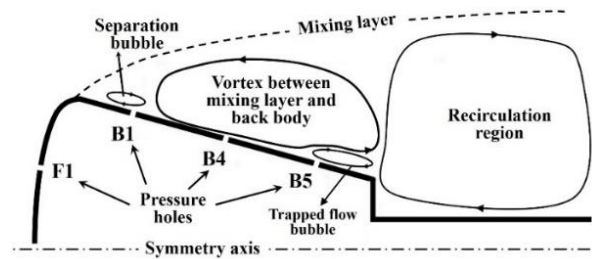


Fig. 7 Flow physics schematic in the back of the model

the vortex region behind the model. Relatively minor adjustments in the angle of attack do not significantly affect the vortex flow conditions behind the model.

Consequently, within these angles, the static pressure on the rear surface can be assumed to remain largely unaffected by changes at the front surface and angle of attack. This observation aligns with Fig. 5 from [Yang and Radespiel \(2017\)](#). Examining the pressure diagram during static testing (Fig. 6) reveals a significant contrast in the vortex section behind the model. Specifically, at Mach 2.2, the pressure coefficient hovers close to zero, while at Mach 2, it dips into the negative domain, indicating pressures lower than the freestream static pressure. Furthermore, higher Mach numbers lead to an increased pressure coefficient in the front section, consistent with the trend in Fig. 5 by [Yang and Radespiel \(2017\)](#).

Figure 7, inspired by [Murman \(2009\)](#) and [Bukhat Khan et al. \(2022\)](#), illustrates the schematic of flow features on the capsule model and the location of pressure taps on the forebody and aftbody. As shown in this figure, a shear layer (mixing layer) separates the freestream supersonic flow and the flow near the surface of the aftbody. The shear layer originates from the connection point of the forebody and aftbody. There is a recirculating region behind the model, which creates a vortex over the forebody of the capsule. The diameter of the model causes the separation bubble to appear in the vicinity of the B1 sensor—similarly, near sensor B5, a bubble forms due to the sharp trailing edge of the model. As the freestream Mach number increases from $M_\infty = 1.8$ to $M_\infty = 2.2$, the strength of the bow shock increases, and the static pressure behind the shock amplifies. The pressure increase forces the shear layer towards the model surface and decreases the region between the mixing layer and the aftbody surface. This leads to the shrinking of the vortex on the model surface and pushes it downstream. So, the pressure of the aftbody surface remains unchanged during the pitching motion.

The outcomes of the dynamic test cases are now discussed. In these instances, the average cycle of the pitching moment is extracted from the balance data, corresponding to oscillations centered on the zero-mean angle of attack. Then, the dynamic stability coefficient is calculated using equation (1). The results are presented in Table 3.

Table 3 presents a discernible trend wherein an escalation in Mach number correlates with an augmented dynamic stability value. However, it is notable that the

Table 3 Dynamic stability coefficients at zero mean angle of attack

M_∞	f (Hz)	3	4	5
1.8		+0.0032	-0.0068	-0.0161
2.0		-0.0331	-0.0369	-0.0694
2.2		-0.0922	-0.1117	-0.1358

dynamic stability value at Mach 1.8 closely approaches the neutral limit and the threshold of dynamic instability. These findings align harmoniously with assertions made by Owens et al. (2011). According to the mission design outlined within this reference, the Drogue chute functions below Mach 2, which primarily serves to rapidly decelerate and navigate through the dynamic instability phase of the capsule, ultimately preparing for the deployment of the main parachute. Moreover, heightened oscillation frequencies within the capsule contribute to an elevation in dynamic stability. Among the contributing factors to this augmentation, a salient aspect is the independence of the vortex region behind the model from oscillations. This phenomenon, recurrent in numerous references, is facilitated by increased oscillation frequency. The primary vortex behind the model attains an autonomous status owing to its steady state and significantly lower frequency of vortex alterations. Simultaneously, the augmentation of the Mach number induces distinct alterations, elucidated by the paired diagrams in Fig. 7 of Kiritani et al. (2020).

This leads to a more confined vortex region behind the model. Consequently, the aftbody vortex relocates farther rearward. Referencing the discourse presented in Table 8 of Li et al. (2022), this displacement of the aftbody vortex, coupled with a reduction in the separation area on the aftbody surface, is a mechanism for enhancing dynamic stability.

Figure 8 provides shadowgraph flow visualizations for Mach numbers 1.8, 2.0, and 2.2 in zero angle of attack in pitching oscillation. The mixing layer in the images is pale and cannot be seen easily, so specified with yellow dotted lines in the figures. A white dotted vertical line is depicted whose length equals the distance between the upper and lower shear layer in $M_\infty = 2.2$. This line shows the increase of the distance of the shear layer with the aftbody surface in lower Mach numbers. This implies that the vortex flow on the aftbody shrinks as the Mach number increases. The horizontal white line is also used to show the bow shock's stand-off distance in different Mach numbers. As shown in Fig. 8, with increasing freestream Mach number from $M_\infty = 1.8$ to $M_\infty = 2.2$, the stand-off distance of the bow shock is decreasing (the white line in front of the model is the stand-off distance of the bow shock in $M_\infty = 2.2$).

Due to the invariable total pressure in the wind tunnel, the pressure behind the bow shock increases as the Mach number decreases. The increasing pressure is one of the reasons for the increase in the stand-off distance of the bow shock, which can also be seen in Fig. 8 (increasing the length of the horizontal white line in front of the model). Increasing the stand-off distance of the bow shock

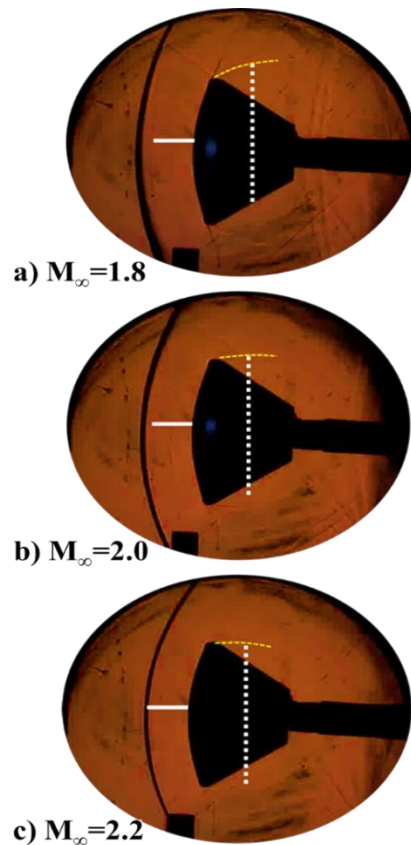


Fig. 8 Mach number effect on general flow phenomena at $f=3$ Hz at zero mean angle of attack

and the total pressure due to the decrease in the freestream Mach number is one of the main factors in reducing the distance of the reflected shock wave from the tunnel wall to the model. As shown in Fig. 8, the reflected shock wave from the tunnel wall is near the model at Mach 1.8. At Mach 2.0, it can be seen at the end of the photo range, but it is not in the picture at Mach 2.2. Also, the pressure of the vortex flow on the aftbody increases as the Mach number decreases.

Figure 9 illustrates the pitching moment coefficient variation in response to changes in the angle of attack, facilitating an exploration of the impact of the Mach number. Notably, the pitching moment coefficient at Mach 1.8 falls within the range defined by the values obtained at Mach 2 and 2.2. A similar trend is notably evident in Fig. 7 of Yang and Radespiel (2017). However, the specific logic underlying this behavior is not explicitly stated in that reference. It can be assumed that this behavior may be attributed to changes in dynamic stability and the expansion of the vortex region on the aftbody surface.

Table 4 shows the reduced frequency values related to the given test conditions. Although the obtained reduced frequency values appear notably small, Teramoto's analysis clarifies that using freestream velocity in the formula $\frac{\omega d_{ref}}{U_\infty}$ inherently yields small values (Teramoto et al., 2001). In contrast, were the velocity of vortex propagation applied, this value would surge by a factor of at least eight. In a parallel context, the

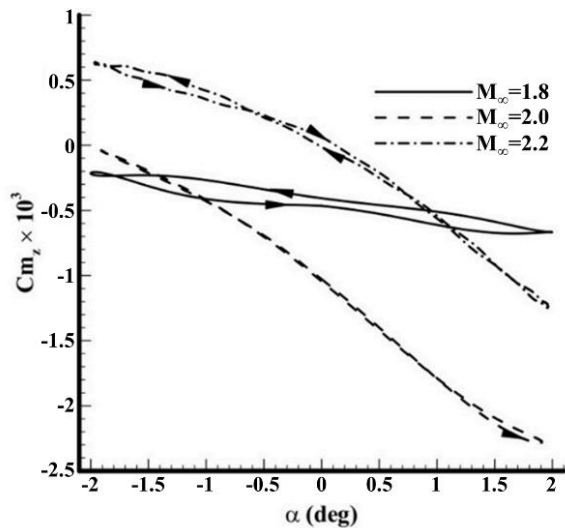


Fig. 9 Change of pitching moment coefficient vs. angle of attack in $f=3$ Hz

Table 4. Reduced frequency corresponding to the test conditions

M_∞	f (Hz)	3	4	5
1.8		0.0047	0.0063	0.0078
2.0		0.0044	0.0059	0.0074
2.2		0.0042	0.0056	0.007

impact of the oscillation frequency parameter is elucidated in Kazemba (2012), where outcomes for an entry geometry at Mach 1.76, featuring a reduced frequency of 0.007, are presented; this geometry oscillates at an approximate rate of 4.5 Hz.

Figure 10 shows time-dependent pressure coefficient measurements obtained during 2-second sampling at sensors F1 and B1 at a frequency of 3 Hz at Mach 2 and Mach 2.2. Figure 11 demonstrates an averaged oscillation cycle of the results shown in Fig 10, portrayed in dimensionless time. For ease of visualization of the data in this figure, the average value of the pressure coefficient in the rear body of the model (B1) was subtracted from the oscillation data. The values on the left side of Fig. 11.b reflect the differential oscillating pressure coefficient between the oscillating pressure coefficient and the average value. The average pressure coefficient at Mach 2 is -0.3117, and at Mach 2.2, it is -0.0365.

Figure 11 provides the cycle-averaged pressure coefficient and its change for pitching motion in two freestream Mach numbers of 2.0 and 2.2. This figure reveals that alterations in the pressure coefficient for the two Mach numbers have almost no phase delay. However, this phenomenon follows a distinctive pattern in the behavior of the B1 sensor. Specifically, the pressure coefficient of B1 initiates the cycle with a small positive value for Mach number 2.0, while this value converges to zero for Mach number 2.2. The discerned disparity at the inception of the Mach 2 cycle can be conceptualized as a manifestation of phase delay, a phenomenon noted in various references, including Teramoto et al. (2001) and

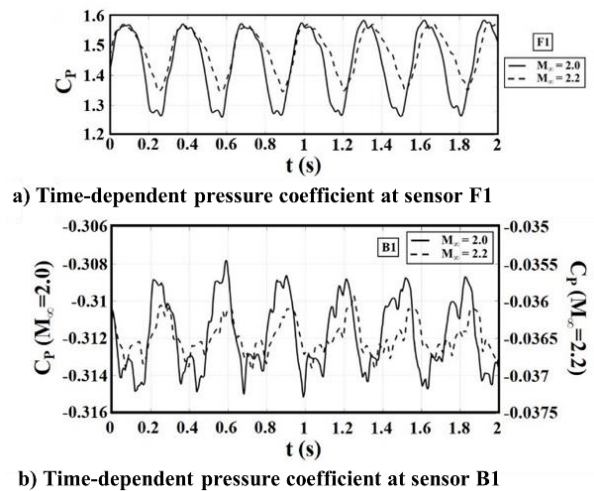


Fig. 10 Time-dependent pressure coefficient in oscillating motion at $f = 3$ Hz

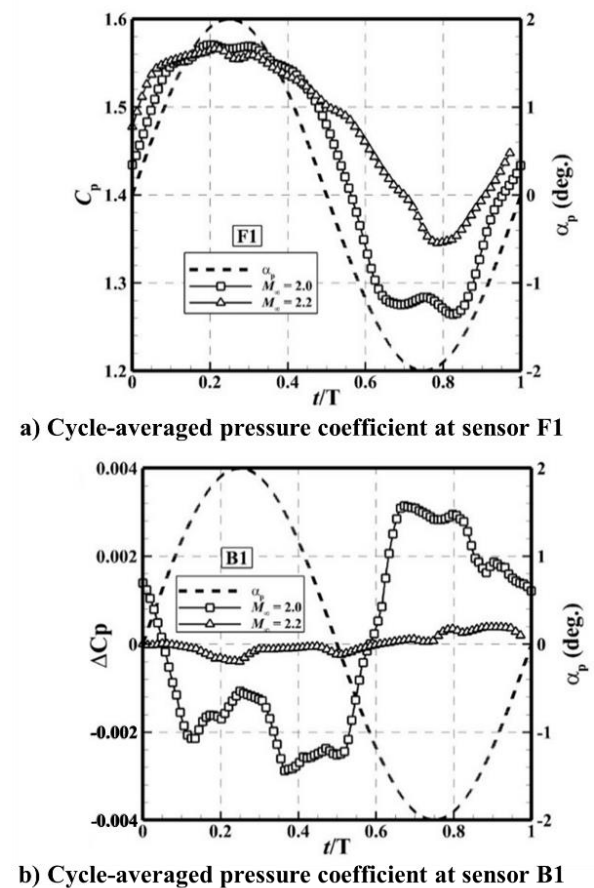


Fig. 11 Changes of pressure coefficient in oscillating motion at $f = 3$ Hz

Kazemba (2012). Furthermore, Fig. 11 implies the relative autonomy of changes in the aftbody pressure sensor at Mach 2.2, considering the minute oscillation range exhibited at Mach 2.0. This relative independence of the pressure coefficient at Mach number 2.2 may be attributed to the reduction in the vortex area on the aftbody surface, as depicted in Fig. 7, alongside the diminution in the

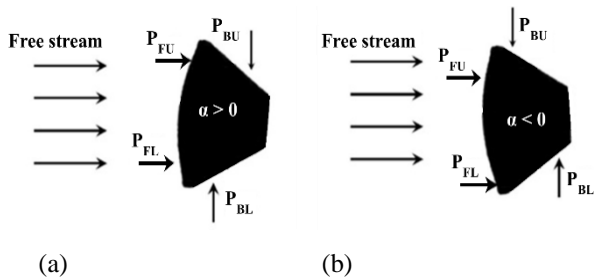


Fig. 12 Schematic of pressure changes around the blunt model in supersonic flow

distance between the mixing layer originating from the maximum diameter and the surface of the aftbody.

Driven by their distinct geometries, entry capsules are classified into two segments regarding flow patterns, as shown in Fig. 12. Across all Mach numbers, the pressure variance in the frontal section of the model imparts an axial force. At a positive angle of attack during oscillation, the pressure at the P_{FU} region is lower than the P_{FL} , generating a torque opposing the oscillation direction around the center of mass. Conversely, under a negative angle of attack, the pressure conditions are reversed, and $P_{FU} > P_{FL}$. Notably, the pressure differentiation between these regions escalates with rising Mach numbers, ultimately augmenting the moment generated by the axial force at elevated Mach levels. However, it is pivotal to acknowledge that a vortex within the aftbody region incites a pressure disparity that manifests as a normal force. Consequently, the moment imposed around the center of mass corresponds to the oscillation direction, constituting a destabilizing moment. At higher Mach numbers, as shown in Fig. 8, the vortex's influence is confined to a smaller section of the aftbody model, consequently diminishing the destabilizing moment. As a result, the cumulative moments contribute toward a stabilization configuration. Conversely, the reduction in Mach number yields a twofold impact. Primarily, the pressure variance within the frontal region recedes due to the attenuated bow shock, consequently depleting the stabilizing moment. Subsequently, the vortex flow engulfs a significant proportion of the aftbody model, intensifying the destabilizing moment. This intricate interplay culminates in the capsule's dynamic instability at low supersonic flows. Addressing this situation requires practical solutions, such as removing the back body or increasing the angle of the aftbody edge. This strategic intervention aims to prevent the formation of vortex flow along the aftbody during supersonic conditions. Notably, the dynamic stability of geometries similar to Soyuz or inflatable entry configurations adheres to these two underlying principles.

An alternative approach to ensuring the stability of such geometries involves implementing an average angle of attack, thereby establishing a consistent stabilizing moment within the frontal section of the body. Alternatively, increasing the oscillation frequency can lead to vortex flow autonomy concerning the rear section oscillation of the model. The results presented in Tables 3 and 5 support the effectiveness of both proposed solutions.

Table 5 Dynamic stability coefficient at the mean angle of attack = 5 °

M_∞ \ f (Hz)	3	4	5
1.8	-0.2069	-0.2873	-0.3716
2.0	-0.2726	-0.3198	-0.433
2.2	-0.4502	-0.5443	-0.6118

Additionally, increasing the oscillation frequency could potentially compromise the live cargo in the capsule. As a result, this solution is usually excluded from design discussions. Therefore, choosing a predetermined average angle of attack or modifying the aftbody geometry is the optimal approach for designing re-entry capsules to transport living cargo safely.

4. CONCLUSION

The dynamic instability region of the Orion return capsule during force pitching oscillation is investigated through wind tunnel experiments. The measured force and surface pressure sensors analyze the flow dynamics and instability. The most pertinent results of current research can be summarized as follows:

1. The flow is in the instability region at Mach numbers less than 2.0 and frequencies less than 4. This instability is visible in the case of $M_\infty = 1.8$ and $f = 3$.
2. The flow becomes more stable as the frequency or angle of attack increases at a constant Mach number.
3. The flow structure in the truncate area behind the model plays a fundamental role in the stability of the capsule. If the aftbody has an inclined surface, vortex flow can be attached to the surface in the low supersonic freestream.
4. The results show that the flow structure in the truncate area behind the model is independent of the angle of attack oscillations as the Mach number increased.
5. As the Mach number increases, the distance between the shear layer and aftbody surface decreases. The flow over the aftbody surface is affected mainly by the shear layer, not the circulating flow behind the model. As a result, in greater Mach numbers, the aftbody surface pressure shows less variation in the pitching motion.
6. As the Mach number decreases, the distance between the shear layer and aftbody surface increases, and the flow is mostly affected by recirculating flow behind the model, resulting in instability. The normal flow over the aftbody surface, which has a destabilizing effect, increases in this case.

The conclusions drawn in this study are perceived by analyzing the experimental results in three Mach numbers: 1.8, 2.0, and 2.2. To further prove the validity and universality of the above claims, more experimental tests, and numerical simulations are aimed at, and these will be performed in the progressing investigations.

ACKNOWLEDGMENTS

Authors can acknowledge the contribution and help of those people or institutes that do not meet the authorship criteria. The responsibility of the information released within this section is completely on the corresponding author. Also, the authors are grateful for the help provided by Mr. S. Dorosti of the Wind Tunnel Group.

CONFLICT OF INTEREST

The authors declare that they have no known competing financial interests or personal relationships that could have appeared to influence the work reported in this paper.

AUTHORS CONTRIBUTION

M. Sargolzaie: Conceptualization, experimentation, Data processing, Formal analysis, Writing-original draft. **Dr. H. Fazeli:** Conceptualization; Supervision, Writing – review & editing. **Dr. M.R. Soltani:** Supervision, and supporting.

REFERENCES

- Adamov, N. P., Kharitonov, A. M., Chasovnikov, E. A., Dyad'kin, A. A., Krylov, A. N., & Aleksandrov, E. N. (2016). Experimental study of aerodynamic characteristics of a reentry vehicle on a setup with free oscillations at supersonic velocities. *Thermophysics and Aeromechanics*, 23, 791-800. <https://doi.org/10.1134/S0869864316060019>
- Benek, J., Buning, P., & Steger, J. (1985). A 3-D chimera grid embedding technique. 7th Computational Physics Conference (p. 1523). <https://doi.org/10.2514/6.1985-1523>
- Bird, J. D., & Reese, D. E. (1958). *Stability of ballistic reentry bodies*. NACA Conference on High-Speed Aerodynamics, March 18- 20, (p. 103). (No. NACA RM-L58E02a).
- Brock, J. M., Stern, E. C., & Wilder, M. C. (2019). Computational fluid dynamics simulations of supersonic inflatable aerodynamic decelerator ballistic range tests. *Journal of Spacecraft and Rockets*, 56(2), 526-535. <https://doi.org/10.2514/1.A34208>
- Bukhat Khan, S., Maqsood, A., Akhtar, S., Xie, D., & Riaz, R. (2022). Causation of supersonic limit cycle oscillations in atmospheric entry vehicles. *Journal of Spacecraft and Rockets*, 59(3), 960-974. <https://doi.org/10.2514/1.A35211>
- Chasovnikov, E. A. (2020). Specific features of the aerodynamic moment and the pitch damping of a re-entry vehicle model exercising free oscillations at supersonic speeds. *Thermophysics and Aeromechanics*, 27, 331-338. <https://doi.org/10.1134/S0869864320030026>
- Cliff, S. E., & Thomas, S. D. (2005). *The Apollo capsule optimization for improved stability and computational/experimental data comparisons* (NASA TM-2005-213457).
- Dayman Jr, B., Brayshaw Jr, J. M., Nelson, D. A., & Babineaux, T. L. (1963). The influence of shape on aerodynamic damping of oscillatory motion during Mars atmosphere entry and measurement of pitch damping at large oscillation amplitudes. *Advances in Astronautical Sciences*, 13, 357.
- Fletcher, H. S. (1960). *Damping in pitch and static stability of supersonic impact nose cones, short blunt subsonic impact nose cones, and manned reentry capsules at Mach numbers from 1.93 to 3.05*. NASA TM X-347.
- Gülhan, A., Klevanski, J., & Willems, S. (2011). *Experimental study of the dynamic stability of the ExoMars capsule*. Proceedings of 7th European Symposium on Aerothermodynamics. Vol.692, p.9. Brugge, Belgian. ISSN 1609-042X.
- Han, S., Lee, B. J., Ahn Furudate, M., & Nagai, H. (2024). Numerical investigation of the dynamic instability of a reentry capsule in transonic flow. *AIAA Journal*, 62(2), 449-459. <https://doi.org/10.2514/1.J063428>
- Jespersen, D., Pulliam, T., Buning, P., Jespersen, D., Pulliam, T., & Buning, P. (1997). *Recent enhancements to OVERFLOW*. 35th Aerospace Sciences Meeting and Exhibit (p. 644). <https://doi.org/10.2514/6.1997-644>
- Kandula, M., & Buning, P. (1994). *Implementation of LU-SGS algorithm and Roe up-winding scheme in OVERFLOW thin-layer Navier-Stokes code*. Fluid Dynamics Conference (p. 2357). <https://doi.org/10.2514/6.1994-2357>
- Kawano, R., Ikami, T., Nagai, H., & Yamada, K. (2024). *Dynamic behavior measurement of new sample return capsule for deep space exploration using transonic wind tunnel*. AIAA SciTech 2024 Forum (p. 2147). <https://doi.org/10.2514/6.2024-2147>
- Kazemba, C., Braun, R., Schoenenberger, M., & Clark, I. (2012). *Dynamic stability analysis of blunt body entry vehicles through the use of a time-lagged aftbody pitching moment*. 51st AIAA Aerospace Sciences Meeting including the New Horizons Forum and Aerospace Exposition (p. 226). <https://doi.org/10.2514/6.2013-226>
- Kiritani, H., Tanaka, N., Ohtani, K., Fujita, K., & Nagai, H. (2020). *Transonic flow field analysis of a free flight capsule using ballistic range*. AIAA SciTech 2020 Forum (p. 1990). <https://doi.org/10.2514/6.2020-1990>
- Li, Q., Zhao, R., Zhang, S., Rao, W., & Wei, H. (2022). Study on dynamic characteristics of Mars entry module in transonic and supersonic speeds. *Space: Science & Technology*. <https://doi.org/10.34133/2022/9753286>
- Liou, M. S., & Buning, P. (2000). *Contribution of the recent AUSM schemes to the OVERFLOW code-*

- Implementation and validation*. 18th Applied Aerodynamics Conference (p. 4404). <https://doi.org/10.2514/6.2000-4404>
- Mark, C. P., & Netto, W. (2023). Determining dynamic stability of a re-entry capsule at free fall. *Aerotecnica Missili & Spazio*, 1-16. <https://doi.org/10.1007/s42496-023-00180-7>
- Matsumoto, S., Kondoh, Y., Nagai, S., Tagai, R., Imada, T., & Nakano, E. (2016). *Aerodynamic oscillation and attitude control analysis for reentry capsule using OREX flight data and wind tunnel data*. AIAA Guidance, Navigation, and Control Conference (p. 1131). <https://doi.org/10.2514/6.2016-1131>
- Murman, S. M. (2009). Dynamic simulations of atmospheric-entry capsules. *Journal of Spacecraft and Rockets*, 46(4), 829-835. <https://doi.org/10.2514/1.41078>
- Nagai, S., Hashimoto, A., Koga, S., Hidaka, A., Murakami, K., Tagai, R., & Hayashi, K. (2021). *Synergistic numerical and experimental investigations of the dynamic stability of a re-entry lifting capsule*. AIAA SciTech 2021 Forum (p. 1107). <https://doi.org/10.2514/6.2021-1107>
- Owens, D. B., & Aubuchon, V. (2011). *Overview of orion crew module and launch abort vehicle dynamic stability*. 29th AIAA Applied Aerodynamics Conference (p. 3504). <https://doi.org/10.2514/6.2011-3504>
- Placco, L., Cogo, M., Bernardini, M., Aboudan, A., Ferri, F., & Picano, F. (2023). Large-eddy simulation of the unsteady supersonic flow around a mars entry capsule at different angles of attack. *Aerospace Science and Technology*, 143, 108709. <https://doi.org/10.1016/j.ast.2023.108709>
- Reding, J. P., & Ericsson, L. E. (1972). Dynamic support interference. *Journal of Spacecraft and Rockets*, 9(7), 547-553. <https://doi.org/10.2514/3.61738>
- Schoenenberger, M., & Queen, E. M. (2008). *Limit cycle analysis applied to the oscillations of decelerating blunt-body entry vehicles*. Symposium AVT-152 on Limit-Cycle Oscillations and Other Amplitude-Limited, Self-Excited Vibrations, NATO, Norway.
- Schrijer, F., & Walpot, L. (2010). *Experimental investigation of the supersonic wake of a reentry capsule*. 48th AIAA Aerospace Sciences Meeting Including the New Horizons Forum and Aerospace Exposition (p. 1251). <https://doi.org/10.2514/6.2010-1251>
- Steketee, D. (1967). *Dynamic stability of space vehicles. Volume 11-Entry disturbance and control* (NACA CR-935).
- Teramoto, S., Hiraki, K., & Fujii, K. (2001). Numerical analysis of dynamic stability of a reentry capsule at transonic speeds. *AIAA Journal*, 39(4), 646-653. <https://doi.org/10.2514/2.1357>
- Tsurumoto, T., Takahashi, Y., Terashima, H., & Oshima, N. (2019). *Numerical analysis of aerodynamic instability for HAYABUSA type reentry capsule*. 8th European Conference for Aeronautics and Space Sciences. <https://doi.org/10.13009/EUCASS2019-288>
- Uselton, B. L., & Cyran, F. B. (1980). *Sting interference effects as determined by measurements of dynamic stability derivatives, surface pressure, and base pressure for Mach numbers 2 through 8* (Vol. 79, No. 89). Arnold Engineering Development Center, Air Force Systems Command, United States Air Force.
- Wei, H., Li, X., Huang, J., Li, Q., & Rao, W. (2021). Ballistic range testing data analysis of Tianwen-1 Mars entry capsule. *Space: Science & Technology*. <https://doi.org/10.34133/2021/9830415>
- Whitlock, C. H., & Siemers III, P. M. (1972). Parameters influencing dynamic stability characteristics of Viking-type entry configurations at Mach 1.76. *Journal of Spacecraft and Rockets*, 9(7), 558-560. <https://doi.org/10.2514/3.61741>
- Willems, S., Gülhan, A., & Esser, B. (2013). Shock induced fluid-structure interaction on a flexible wall in supersonic turbulent flow. *Progress in Flight Physics*, 5, 285-308. <https://doi.org/10.1051/eucass/201305285>
- Yang, X., & Radespiel, R. (2017). Longitudinal aerodynamic performance of the Apollo entry capsule near transonic speeds. *Journal of Spacecraft and Rockets*, 54(5), 1100-1109. <https://doi.org/10.2514/1.A33609>